

Research Paper

Additively manufactured electromagnetic based planar pressure sensor using substrate integrated waveguide technology

Yeonju Kim^{a,1}, Yepu Cui^{b,1}, Manos M. Tentzeris^b, Sungjoon Lim^{a,*}

^a School of Electrical and Electronics Engineering, Chung-Ang University, Seoul, 06974, Republic of Korea

^b School of Electrical and Computer Engineering, Georgia Institute of Technology, Atlanta, GA, 30332, USA



ARTICLE INFO

Keywords:

Electromagnetic based sensor
Pressure sensor
Substrate integrated waveguide
3D printing
Inkjet printing
Additive manufacturing

ABSTRACT

This paper proposes an electromagnetic based planar pressure sensor using a substrate integrated waveguide (SIW). The proposed pressure sensor is inspired by a rectangular SIW cavity and is additively manufactured using 3D printed dielectric material with inkjet printed conductive pattern. Since the resonance frequency depends on the SIW centre in transverse electrical mode, a circular cylinder with four bridges is placed at the SIW centre for perturbation. We inserted meshed material at the SIW centre, to facilitate soft pressing, and simplify producing frequency shifts due to capacitive coupling perturbation from different pressure levels. The proposed concept was numerically and experimentally verified, reducing resonance frequency from 4.28 to 3.71 GHz by increasing the pressure from 0 to 2.4 kPa. Device sensitivity = 2.4×10^8 Hz/kPa, and stable frequency change was observed over 100 repeats.

1. Introduction

With the establishment of 5th generation (5G) wireless networks, research on internet of things (IoT), connecting various objects wirelessly, has further accelerated. IoT technology is based on integrating sensors, radio frequency identification (RFID) tags, communication, and information processing systems [1–3]. Sensors detect physical properties, such as force, strain, pressure, displacement, etc.; and the signal is transmitted to the communication system via RFID tags. Among various sensors, conventional pressure sensors incorporate either capacitor or piezoelectric based sensors [4–6], which provide high sensitivity to signal voltage changes but require external DC power supply for operation; whereas EM based passive pressure sensors offer simplified, low cost, robust structures, without requiring an additional power supply [7]. RFID technology [8–11], the foundation for IoT, identifies and monitors signals using radio waves. These are critical IoT issues, as least as important as subsequent processing of the data transmitted to the communication system. Therefore, electromagnetic based cost-effective EM based sensors [12–15] are essential to meet growing research, industrial, and consumer demands for RFID and IoT technologies.

Additive manufacturing techniques, including 3D printing and inkjet printing, are being increasingly applied to fabricate sensors [16,17] because they enable creating customized sensor prototypes. The most

commonly used 3D printing methods [18–21] for sensor manufacturing include fused deposition modelling (FDM) and stereolithography apparatus (SLA). FDM printing creates the desired structures by extruding materials, such as thermoplastics, glass, and ceramics. However, although FDM offers simplicity and easy access, it has relatively low resolution. In contrast, SLA printing is based on photo-curing using a photopolymer and offers relatively fine resolution structures [22]. Despite the limited range of printing materials, resin properties can create flexible and stretchable structures. Inkjet printing [23,24], another additive manufacturing technology, creates circuit components by precisely depositing functional ink onto various substrates, including paper, polyethylene terephthalate (PET), polyimide, etc. This can be utilized to fabricate multilayer designs and enables low cost and rapid prototyping compared with conventional printed circuit board (PCB) etching.

Pressure sensors to measure pressure or structural loading variations have also been fabricated by 3D and inkjet printing [25–29]. For example, flexible pressure mapping sensors to measuring central plantar pressure using capacitive sensing [30]. Sensor electrodes have been developed using printed conductive ink Poly (3,4-ethylenedioxythiophene)-poly (styrenesulfonate) on flexible thermoplastic elastomer (TPU) with low Young's modulus. Array sensors on flexible PCB can achieve linearity and sensitivity. However, sensor assembly needs improvement due to flexible PCB vulnerability used to connect each

* Corresponding author.

E-mail address: sungjoon@cau.ac.kr (S. Lim).

¹ Both authors contributed equally to this work.

sensor for an array. A 3D printed Fiber Bragg grating (FBG) pressure sensor has also been constructed [31] by embedding a bare FBG sensor inside polylactic acid (PLA) material using material extrusion additive manufacturing. This sensor offers multiplexing, high sensitivity, and light weight, despite significant wavelength fluctuation from the printing process. A 3D and inkjet printed force/pressure sensing device has also been reported [32], based on capacitive sensing employing two diaphragm types fabricated from 3D printed steel and 3D printed ceramics, fabricated by blinder jetting and lithography based ceramic manufacturing (LCM), respectively. Sensor electrodes were also fabricated by inkjet printing. Although this sensor achieved high sensitivity with low excitation signal, thinner membranes are required for better characteristics.

This paper proposes an electromagnetic based planar pressure sensor using a substrate integrated waveguide (SIW). The proposed pressure sensor was inspired by a rectangular SIW cavity resonator and additively manufactured using 3D printed dielectric material and inkjet printed conductive patterns. Since its resonance frequency is dependent on the SIW centre in transverse electrical (TE)₁₀₁ mode, a circular cylinder with four bridges was placed at the SIW centre for perturbation. Capacitive coupling perturbations can produce frequency shifts at different pressure levels. Therefore, the 3D printed solid resin used for the SIW cavity was thicker than that of the microstrip line to help achieve deeper pressing, and we placed meshed material at the SIW centre to facilitate soft pressing. The proposed concept was numerically and experimentally verified using S parameters.

2. Proposed pressure sensor design

Fig. 1 shows the proposed electromagnetic based SIW pressure sensor consists of an SIW cavity resonator and microstrip line. The resonance frequency depends on the effective dielectric constant of SIW cavity, and hence can be changed by altering the pressure. A circular cylinder was loaded on the top of the SIW (Fig. 1(a)) to press into the SIW cavity centre. The circular cylinder has diameter D_s and is connected by four $W_b \times L_b$ bridges. The SIW cavity was realized by 3D printed solid resin and the circular cylinder by 3D printed meshed resin (Fig. 1(b)). The meshed structure ensures the SIW cavity centre can be easily deformed by pressing the circular cylinder. Dielectric materials were fabricated using FLGR02 (Formlabs, USA) resin in a 3D printer. The printed solid resin had dielectric constant $\epsilon_r = 4$ and tangential loss $\tan \delta = 0.07$; whereas the 3D printed meshed resin had $\epsilon_r = 1.2$ and $\tan \delta = 0.01$. The conductive patterns were inkjet printed using silver nanoparticle ink, with conductivity $= 8 \times 10^6$ S/m. An SU-8 layer ($\epsilon_r = 3$, $\tan \delta = 0.04$) was inkjet printed onto the 3D printed material to reduce solid resin surface roughness and improve silver nanoparticle ink adhesion. The proposed sensor ground was fabricated using copper tape.

The resonance frequency for the TE₁₀₁ mode SIW cavity resonator

can be expressed as [33]

$$f_{101} = \frac{c}{2\pi\sqrt{\epsilon_r\mu_r}} \sqrt{\left(\frac{\pi}{W}\right)^2 + \left(\frac{\pi}{L}\right)^2} \quad (1)$$

where c is the speed of light; μ_r and ϵ_r are dielectric material permeability and permittivity inside the cavity, respectively; and W and L are the waveguide cavity resonator effective width and length, respectively.

To decide initial SIW cavity width and length, we set W_{wg} and L_{wg} as initial cavity parameters. When relative permittivity $\mu_r = 1$ and $W_{wg} = L_{wg}$, resonance frequency can be determined from the dielectric constant and W_{wg} . Initially, we assumed the effective dielectric constant of the SIW cavity $= 2.2$ from the geometric mean ($\sqrt{4 \times 1.2} \approx 2.2$) of the two dielectric constants (4 for solid resin and 1.2 for meshed resin). Since we inserted the meshed cylinder in the centre of SIW cavity where the strongest electric field is generated, we considered the dielectric constant from both meshed and solid resin. Therefore, we set $W_{wg} = L_{wg} = 33.3$ mm from Eq. (1), and simulated the initial SIW cavity using ANSYS HFSS. For practical realization, we must include via walls, meshed cylinder, and ramped microstrip feeding line, which will alter the resonance frequency and impedance. Therefore, we optimized the SIW cavity geometry with $W_{SIW} = 32$ mm and $L_{SIW} = 31.7$ mm to achieve impedance matching to 50 ohms. The SIW cavity resonance frequency changed slightly after impedance matching, to 4.28 GHz.

Resonance frequency can be changed by varying dielectric constant of SIW cavity with the given W_{SIW} and L_{SIW} . The proposed sensor design changes effective dielectric constant of SIW cavity by applying pressure. For example, the dielectric constant increases with consequentially dense meshed resin as higher pressure is applied, and resonance frequency is reduced as effective dielectric constant of SIW cavity increases. We calculated the resonance frequency of the SIW cavity from Eq. 1. Because the pressure is applied only to the meshed cylinder of SIW cavity, we extracted the resonance frequency based on input impedance which is converted from S-parameters at different applied pressure [33,34].

Via diameter (D) and SIW cavity pitch (P) were derived as [35]

$$D < \frac{\lambda_g}{5} \quad (2)$$

and

$$P < 2D \quad (3)$$

where λ_g is the SIW cavity guided wavelength. SIW cavity vias are generally kept small to reduce leakage from the cavity. We set $D = 4$ mm and $P = 5.4$ mm, and implemented the via array using inkjet printing.

Fig. 2 shows the circular cylinder to be pressed. Minimum thickness for stable 3D printing to support a circular cylinder was cylinder total height $= 2.8$ mm, with $H_s = 0.8$ mm thick solid resin and $H_m = 2$ mm

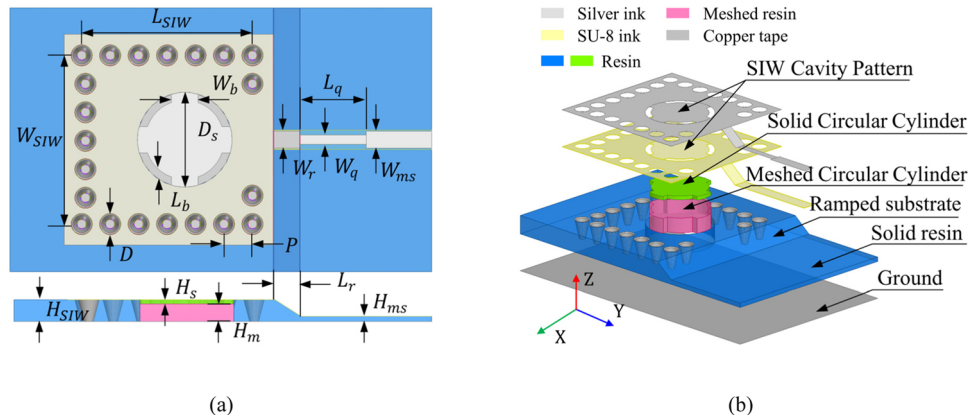


Fig. 1. Proposed SIW cavity pressure sensor (a) top and (b) perspective view.

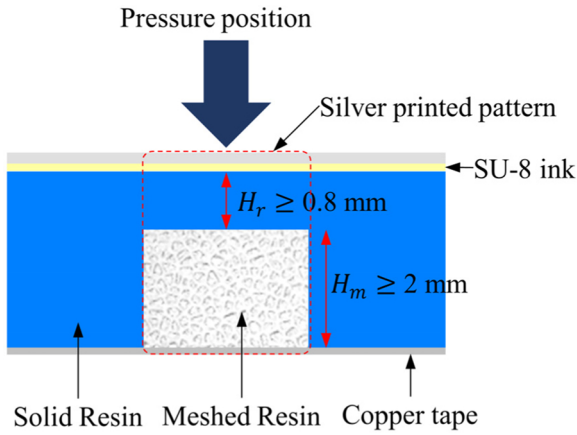


Fig. 2. Circular cylinder to press the proposed SIW cavity sensor (side view).

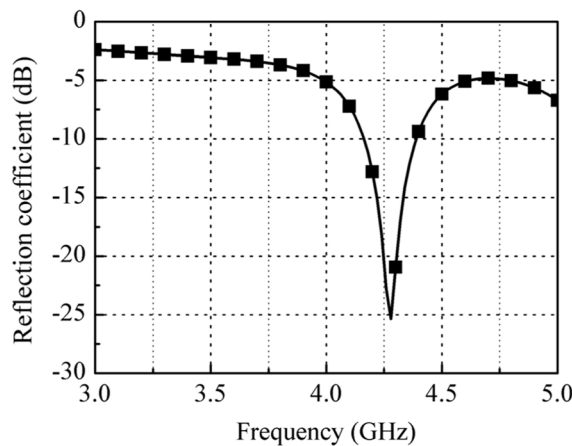
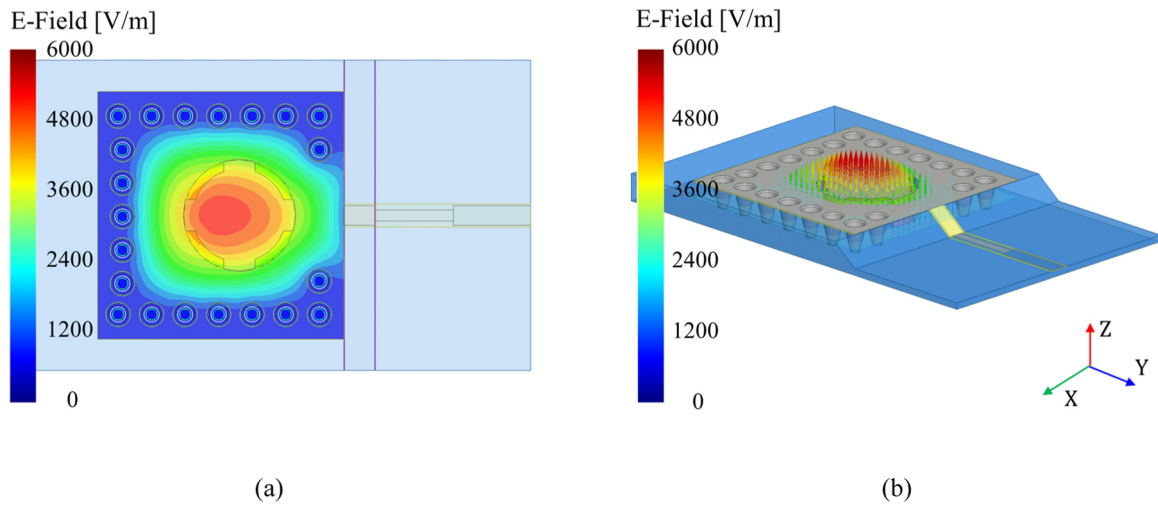
thick meshed resin. Cylinder height decreases when it is pressed due to deformation. Cylinder size and location were determined from the electric field (E-field) distribution in the TE₁₀₁ mode SIW cavity, as shown in Fig. 3(a) and (b) at resonance frequency (4.28 GHz). We used the ANSYS high-frequency structure simulator [36] for EM analysis and

determined optimal cylinder diameter $D_s = 18$ mm to ensure strong E-field distribution. Consequently, bridge dimension was 5×1.5 mm ($W_b \times L_b$) for effective capacitive coupling. The meshed cylinder becomes denser as pressure applied to the SIW cavity cylinder increases, reducing H_m and increasing the dielectric constant. These changes increase capacitance between ground and the cylinder conductive pattern from Eq. (4),

$$C = \epsilon_r \epsilon_0 A / d \quad (4)$$

where ϵ_r and ϵ_0 are material and free space dielectric constants, respectively; A is the conductor area; and d is the separation between the conductors. Thus, the effective dielectric constant of SIW cavity increases and change capacitive coupling is induced at higher pressure, reducing the resonance frequency.

Total SIW cavity height $H_{SIW} = H_s + H_m + H_{SU} = 5.1$ mm, where $H_s = 1$ and $H_m = 4$ mm for stable 3D printing and effectively deeper pressing, respectively; and we set $H_{SU} = 0.1$ mm considering inkjet printing conditions. Because total SIW cavity height is too thick to design a microstrip line for coupling between the SIW cavity and feed, we set microstrip line substrate height $H_{ms} = 1.2$ mm and feed line width $W_{ms} = 3.2$ mm for 50Ω impedance. We inserted a ramped substrate surface between the microstrip line and SIW to smooth the height difference: inclined length $L_r = 5$ mm and width $W_r = 3.2$ mm (as per



(c)

Fig. 3. Simulation results for the proposed SIW pressure sensor: (a) electrical field (E-Field) magnitude at 4.28 GHz, (b) E-Field vector at 4.28 GHz, and (c) reflection coefficient.

Table 1
Design parameters for the proposed SIW pressure sensor.

Parameter	W_{SIW}	L_{SIW}	H_{SIW}	D	P	D_s	L_b	W_b
Value (mm)	32	31.7	5	4	5.4	18	1.5	3.2
Parameter	L_r	W_r	L_q	W_q	H_s	H_m	H_{ms}	W_{ms}
Value (mm)	5	3.2	12.6	1.8	1	4	1.2	3.2

the microstrip line). A quarter wavelength transformer was inserted between the inclined line and 50 Ω feed line to match impedance, with dimension $W_q \times L_q = 1.8 \times 12.6$ mm. Table 1 lists the proposed pressure sensor geometrical parameters, and Fig. 3(c) shows the corresponding S parameter with respect to frequency. The device resonates at 4.28 GHz with -25.5 dB reflection coefficient.

The relationship between meshed cylinder height of SIW sensor and pressure level was derived using COMSOL Multiphysics,

$$\text{Pressure (MPa)} = \text{Weight (kg)} / \text{Area (cm}^2\text{)} \quad (5)$$

We applied pressure on the SIW by loading the cylinder with Korean coins. Hence applied pressure could be directly calculated from the coin weight (1.22 g) and diameter (18 mm). We used five samples: 10, 20, 30, 40, and 50 coins; corresponding to 0.48, 0.96, 1.44, 1.92, and 2.4 kPa, respectively. Table 2 shows material electrical and mechanical properties used in the SIW cavity. We used the transmission line technique [37] to characterize ϵ_r and $\tan \delta$ for the resin. The measured S-parameters showed that solid resin has $\epsilon_r = 4$ and $\tan \delta = 0.07$, and meshed resin has $\epsilon_r = 1.2$ and $\tan \delta = 0.01$. To characterize Young's modulus for solid and meshed resin, we measured tensile strength using a universal testing machine INSTRON 5569, as shown in Fig. 4(a). Fig. 4(b) shows the stress-strain curves of solid and meshed resin. We used the same thickness sample as the circular cylinder in the sensor. We calculated Young's modulus by applying force with 1 mm/min to a solid resin sample and 0.2 mm/min to a meshed resin sample because of different mechanical properties of the solid resin and meshed resin. Because the structural properties of the solid resin and meshed resin are different, we applied the force with a different ratio [38]. Young's modulus of solid resin and meshed resin is 4.4 MPa and 0.77 MPa, respectively. FLGR02 flexible resin was simulated based on 80A durometer rubber, using Poisson's ratio = 0.45, from [39–41] for solid resin and meshed resin [38,41]. Based on measured Young' modulus, we set the effective medium for the meshed resin in COMSOL. Therefore, ΔH of the meshed cylinder at different pressure level can be estimated from COMSOL. These characteristics were used to calculate height changes under different pressures using finite element method (FEM) simulation by COMSOL Multiphysics and HFSS.

Fig. 5 shows SIW cavity cylinder height change (ΔH) with respect to pressure. Since the SIW cavity resonator was symmetric, we used quarter of the structure for efficient structural analysis considering boundary conditions.

Uniformly increasing pressure with 0.48 kPa step was applied to the sensor surface (Fig. 4(a), dashed line) and the pressure sensor was set to linear elastic material. Fig. 5(a) shows height change, ΔH , for 1.92 kPa pressure applied to proposed sensor's cylinder. Since pressure applied to the sensor centre would become larger for structural characteristic, this confirmed that height change occurred predominantly in the centre

Table 2
Electrical and mechanical properties for materials used in the SIW cavity.

	Solid resin	Meshed resin
Dielectric constant (ϵ_r)	4	1.2
Dielectric loss ($\tan \delta$)	0.07	0.01
Young's modulus (MPa)	4.4	0.77
Poisson's ratio	0.45	0.45

of the cylinder. Fig. 5(b) shows simulated results for cylinder height change with respect to pressure, i.e., circular cylinder mechanical deformation under different pressures.

We used ANSYS HFSS [36] to simulate and analyse pressure sensor frequency shifts corresponding to different pressures based on COMSOL Multiphysics simulation outcomes. Cylinder height change, ΔH , related to mechanical deformation, was analysed for different pressures using COMSOL, and the derived relationship used in ANSYS HFSS. When the circular cylinder was deformed with different ΔH depending on pressure, the different height of both meshed resins and coins was also applied to the simulation setup. The dielectric constant also changes when the meshed resin shrinks with higher pressure. Since there were considerable mesh allocation and inefficient computer memory load for meshed resin analysis, we considered the meshed resin as effective solid resin with dielectric constant = 1.2 in HFSS. And we calculated the meshed resin variable effective dielectric constant from the filling ratio [42–44]. Its variable dielectric constant at different ΔH can be also estimated by

$$\epsilon_{r,\text{mesh}} = \epsilon_{r,\text{solid}} \left(\frac{V_{\text{mesh}}}{V_{\text{solid}}} \right) + \epsilon_{r0} \left(1 - \frac{V_{\text{mesh}}}{V_{\text{solid}}} \right), \quad (6)$$

where V_{mesh} and V_{solid} are meshed resin and solid resin volume, respectively; $\epsilon_{r,\text{solid}}$ and ϵ_{r0} are the relative permittivity of solid resin and air, respectively. For instance, we first obtained ΔH from COMSOL and generated the meshed resin cylinder depending on ΔH by using the Voronator web application [45]. After importing it to ANSYS HFSS, its volume (V_{mesh}) for filling ratio can be calculated from the model analysis in ANSYS HFSS. Finally, we derived $\epsilon_{r,\text{mesh}}$ from Eq. (6). Fig. 6(d) shows the calculated effective dielectric constant of the meshed resin which is varied from 1.26 to 1.34 when ΔH is changed from 0.3 to 1.5 mm, respectively. The fitted curve is estimated as $y = 0.0513x + 1.25$.

Fig. 6 (a) shows the proposed EM based pressure sensor with coins placed to apply pressure. Each coin comprises 48 % copper and 52 % aluminium, hence we used conductivity = 5×10^7 S/m for simulation. Fig. 6(b) and (c) show reflection coefficients and frequency shifts with respect to different ΔH . The proposed sensor resonance frequency decreased from 4.21 to 4.14, 4.05, 3.92 and 3.79 GHz as ΔH increased from 0.29 to 0.6, 0.91, 1.21 and 1.5 mm, respectively. Capacitive coupling occurs since ΔH induces higher effective dielectric constant in the SIW cavity, and resonance frequency decreases as dielectric constant increases.

3. Proposed pressure sensor additive manufacturing

Fig. 7 shows the proposed SIW cavity pressure sensor fabrication process comprises

- 3D printed flexible dielectric substrate,
- inkjet printed SU-8 buffer layer to reduce surface roughness, and
- inkjet printed conductive pattern using silver nanoparticle ink.

For 3D printing consistency, we used a laser based stereolithography 3D printing method with Formlabs commercialized 3D printing system. Printing temperature and light intensity were precisely controlled to ensure consistent results. The resin was commercially available, hence had consistent material properties. Structures were printed with 25–300 μm layer thickness resolution. Overall printing time depended on layer thickness, e.g. printing time reduced by approximately 1 h for 100 μm layer thickness compared with 50 μm layer thickness resolution. However, we also need a peel off operation for each printed layer as well as overall printing time. Since SLA printing forms a support structure while printing the sample, the sample must be printed with slight angle to reduce printing per layer, which improves accuracy, but thicker layers will have increased surface roughness.

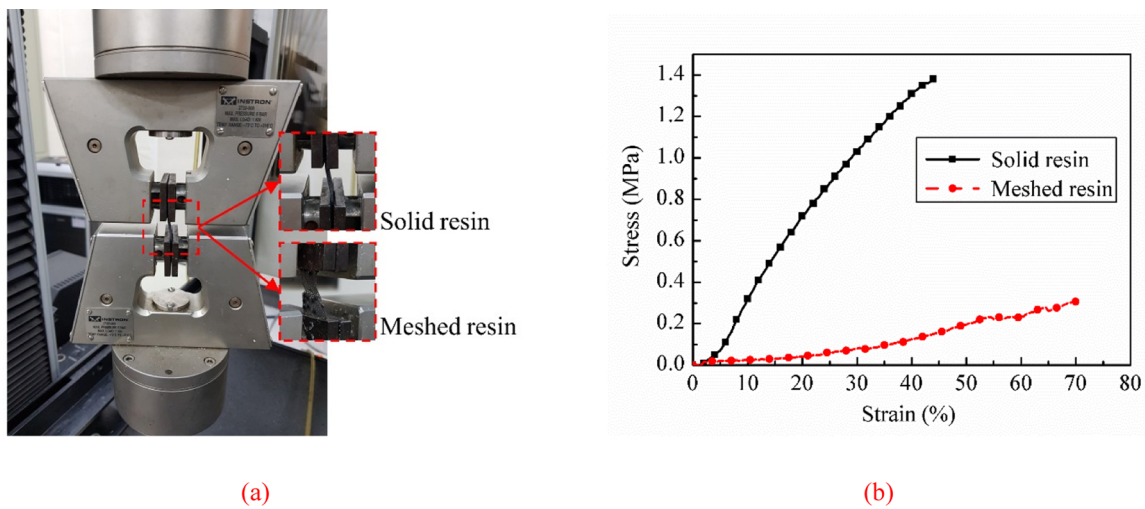


Fig. 4. (a) Tensile strength measurement setup to characterize Young’s modulus of the solid resin and meshed resin. (b) Measured stress-strain curves of the solid resin and meshed resin.

Therefore, we used fixed 50 μm layers at 30° printing angle and fixed position for support materials to provide proper surface roughness for inkjet printing. This ensured accurate printed shape and dimension.

The dielectric solid resin was fabricated using a Formlabs Form 2 SLA 3D printer with Formlabs FLGR02 flexible photopolymer resin, which has 7.7–8.5 MPa tensile strength, 80 % elongation [46], and $\epsilon_r = 4.00$, $\tan \delta = 0.07$ at 4 GHz. The substrate was fabricated with 50 μm layer resolution and post processed with Formlabs wash and cure system. 3D printed samples generally come out of the printer covered with uncured resin, hence we washed the samples for 15 min in 99 % isopropyl alcohol (IPA) to remove the resin, ensuring better accuracy and reducing surface roughness. The washed resin was then cured under 405 nm LED light at 60°C for 60 min to maximize material structural properties, improve consistency, and reduce electromagnetic losses due to insufficient cross linking. The wash-and-cure post processing cleaned left over resin and fully cured the sample, ensuring consist dielectric properties and print quality.

The substrate was 3D printed with 50 μm resolution and presented a relatively smooth surface after washing and curing. However, all 3D printed surfaces have periodic “hills” and “valleys” perpendicular to the plane because the object is printed layer by layer. These substrates

exhibited surface roughness root mean square (RMS) = 6.5 μm (measured with KLA Tencor Alpha-step D-100 stylus profilometer), which is significant compared with a single silver nanoparticle ink layer ($\sim 0.8 \mu\text{m}$). Therefore, we printed 4 MicroChem SU-8 dielectric ink layer as a buffer to smooth the surface [47]. Fig. 8 shows this process reduced surface roughness to RMS = 1.3 μm , which was sufficient for silver nanoparticle printing. We also ensured the printed SU-8 went through a full cure process: soft bake at 95°C for 5 min, 254 nm light @300 mJ/cm², and hard bake at 95°C for 10 min.

Five silver nanoparticle (SNP) conductive pattern layers were inkjet printed with SunChemical EMD5730 silver nanoparticle (SNP) ink using a Dimatix 2800 inkjet printing system at 20 μm drop spacing (1270 dpi) to provide good consistency and conductivity. We applied 90 s UV ozone treatment prior to SNP printing to improve substrate surface wettability without losing too much resolution. Typically, SNP is sintered above 180°C but high temperatures can damage and deform 3D printed substrates, causing cracks and discontinuities for metallic patterns [48]. Therefore, we employed a low temperature gradient sintering process. After SNP printing, samples were placed on a hot plate ramping from room temperature to 90°C at 150°C/h , then held at 90°C for 60 min to completely dry the SNP. Temperature was then

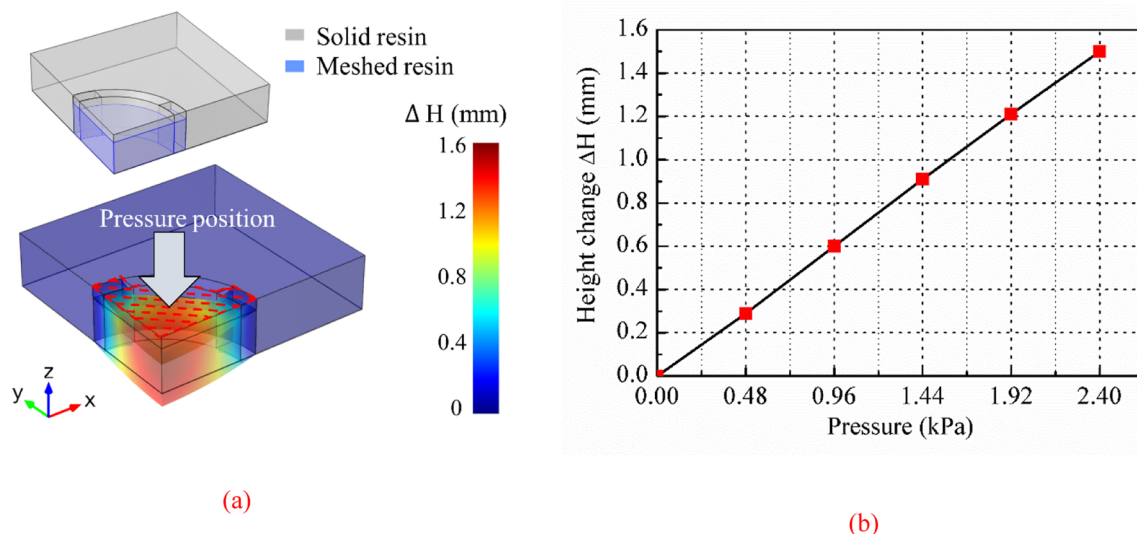
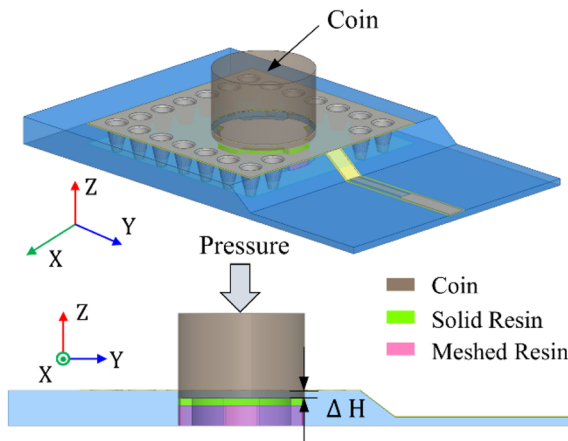
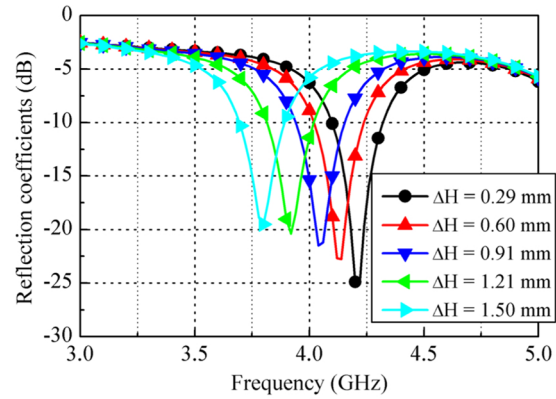


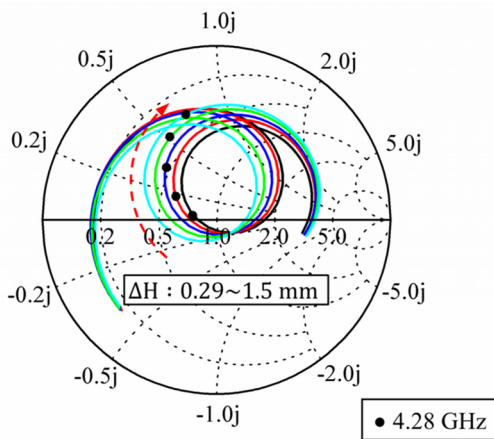
Fig. 5. (a) Height change (ΔH) distribution for 1.92 kPa, and (b) ΔH for the circular cylinder with respect to pressure.



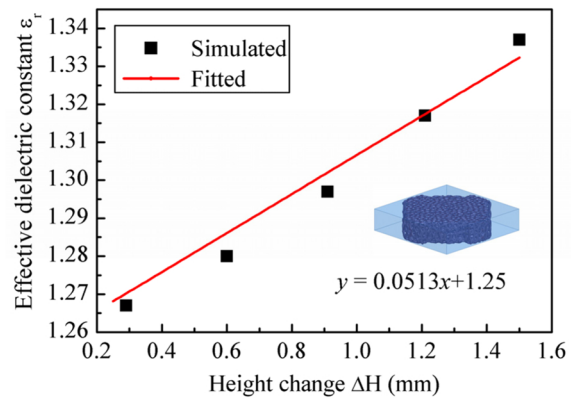
(a)



(b)



(c)



(d)

Fig. 6. Electromagnetic (EM) simulation results for the proposed sensor with respect to ΔH : (a) proposed EM based pressure sensor with coins on the cylinder in perspective and side view; (b) simulated reflection coefficients with respect to ΔH ; (c) Smith chart showing real and imaginary reflection coefficients with respect to ΔH ; and (d) relationship between the meshed resin effective dielectric constant and height change with fitted curve.

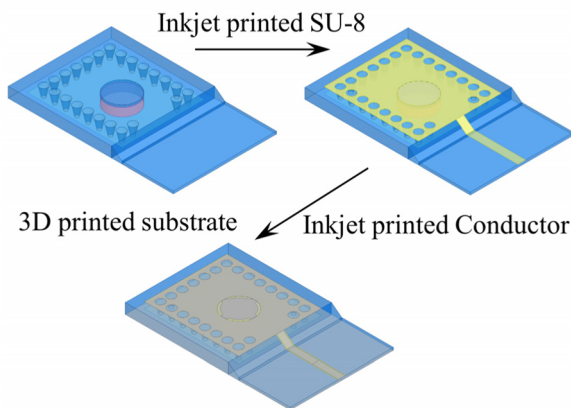


Fig. 7. Three step fabrication process for the proposed SIW cavity pressure sensor.

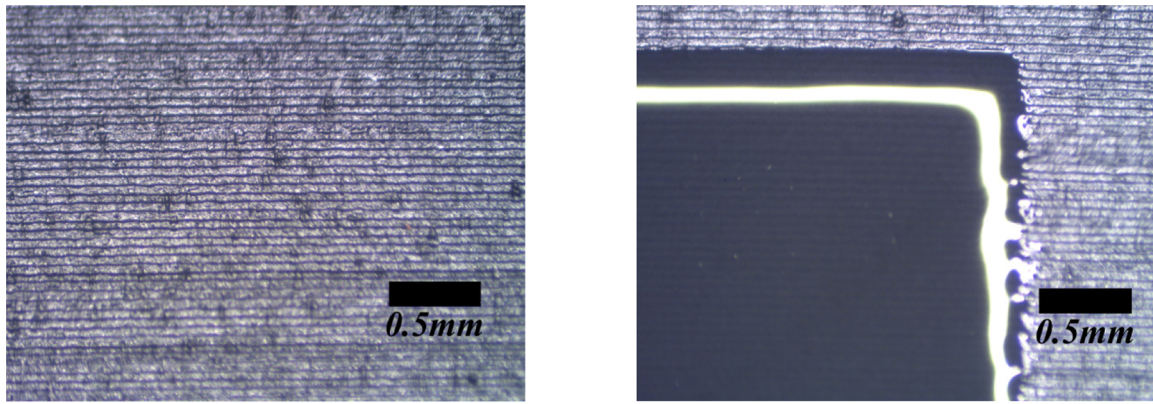
raised to 120 °C at 150 °C/h and held for 15 min to sinter the SNP without breaking the substrate. Finally, we cooled the sample to 30 °C at 150 °C/h to avoid deformation due to rapid temperature change. This sintering process produced a smooth conductor surface with good

conductivity, 8×10^6 S/m.

4. Measurement results and discussion

Fig. 9(a) and (b) show the fabricated EM based SIW pressure sensor. The meshed cylinder was fabricated separately and inserted in the centre of the SIW cavity (Fig. 9(a)). The fabricated sensor reflection coefficients were measured using an Anritsu MS2038C network analyser.

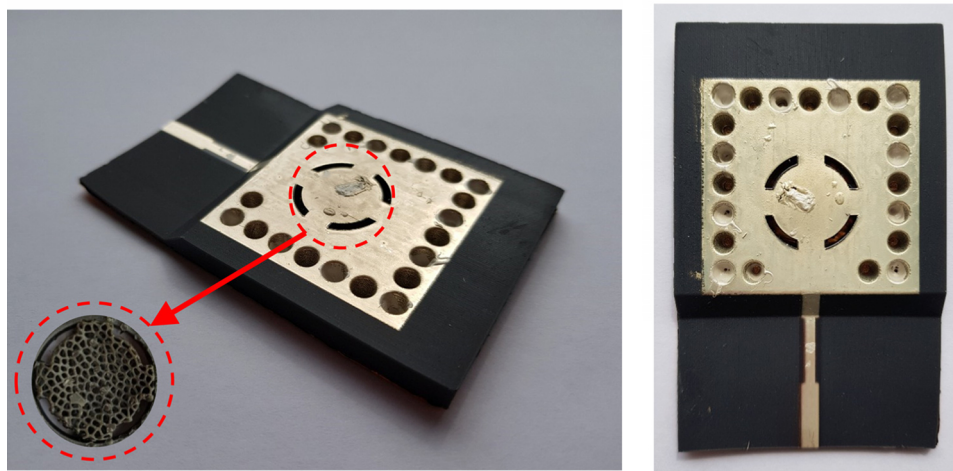
Fig. 10(a) shows measured reflection coefficients with respect to pressure. As discussed above, the various pressure levels were achieved by loading different numbers of Korean coins on the SIW cylinder, increasing pressure by 0.48 kPa for every 10 coins. Resonance frequencies were 4.28, 4.23, 4.16, 4.08, 3.86 GHz, and 3.71 GHz with reflection coefficient -24.1 , -37.4 , -31.5 , -18.8 , -28.5 , and -22.5 dB for 0, 0.48, 0.96, 1.44, 1.92, and 2.4 kPa, respectively. Fig. 10(b) shows that simulated and measured resonance frequencies with respect to pressure level. The slight difference between simulated and measured frequencies results from larger deformation of the meshed resin at higher pressure level. Fig. 10(c) and (d) show measured reflection coefficients and resonance frequencies, respectively, for 1.92, 2.4, and 2.64 kPa to find the proposed sensor break point. The sensor shows consistent resonance frequencies (3.86 and 3.71 GHz) and reflection coefficients



(a)

(b)

Fig. 8. 3D printed solid resin (a) without and (b) with SU-8 buffer layer.



(a)

(b)

Fig. 9. Fabricated EM based SIW pressure sensor (a) perspective view with meshed resin and (b) front view.

(0.035 and 0.071) for 1.92 and 2.40 kPa pressure, respectively. However, the reflection coefficient changed from 0.22 to 0.31 and resonant frequency from 3.2 to 3.61 GHz when 2.64 kPa was applied to the pressure sensor. Thus, the proposed sensor limit (break point) = 2.64 kPa pressure.

Fig. 11 shows that the fabricated SIW sensor exhibited acceptable dynamic stability. We increased pressure from 0 to 2.4 kPa with 0.48 kPa step, then removed the pressure and repeated. Resonance frequency after 1 cycle = 4.27 GHz with -22.2 dB reflection coefficient, compared with initial resonance frequency = 4.28 GHz with -24.1 dB reflection coefficient.

Fig. 12 shows extended repeatability test results for the proposed sensor. Reflection coefficients were measured while repeatedly applying 0.48 and 1.44 kPa to the sensor, i.e., we applied 0.48 kPa and measured the reflection coefficient, and then applied 1.44 kPa and measured the reflection coefficient. Resonance frequency did not change significantly up to cycle 15 with corresponding 1–2 dB reflection coefficient variation. Fig. 12(c) shows that sensor repeatability reduced from approximately cycle 90 and was completely gone after cycle 100.

Fig. 13(a) shows resonance frequency with respect to pressure for the fabricated sensor. The fitted curve was estimated as $y = -0.240x + 4.34$ (GHz) based on polynomial curve fitting, and hence

sensitivity = 2.4×10^8 Hz/kPa. Fig. 12(b) shows fabricated sensor RMS error with respect to pressure. RMS varies from 0.0065 to 0.0150 for 0–2.4 kPa applied pressure.

Table 3 compares the proposed and other RF pressure sensors [12–15]. The proposed sensor exhibits good linearity and sensitivity despite its small dynamic range compared to the other sensors. Moreover, fabrication was significantly simpler than the comparison sensors, utilizing additive manufacturing, and hence the proposed sensor could be swiftly implemented at low cost. Li et al. [12] fabricated a pressure sensor requiring sintering more than 20 h and the pattern was implemented by silkscreen printing using platinum ink. Luo et al. [13] fabricated the sensor using several materials, including Zn/Fe layer, PLLA, and Kapton film using lithography, a considerably more complicated and expensive process than the proposed sensor. Xue et al. [15] fabricated a sensor involving somewhat complicated processing, forming several SU-8 layers by etching and process Au/Cr layer.

The core additive fabrication process we used was very low cost. Inkjet printing costs ~ 0.0001 \$/cm², whereas lithography can cost from 0.03–3 \$/cm² [49]. 3D printing also eliminates requiring a mould for each design, and is ideal to realize complex structures, such as the 3D meshed support in our design. Finally, additive manufacturing fabricates devices by stacking materials into layers without requiring by-products or significant waste materials, hence effectively reducing

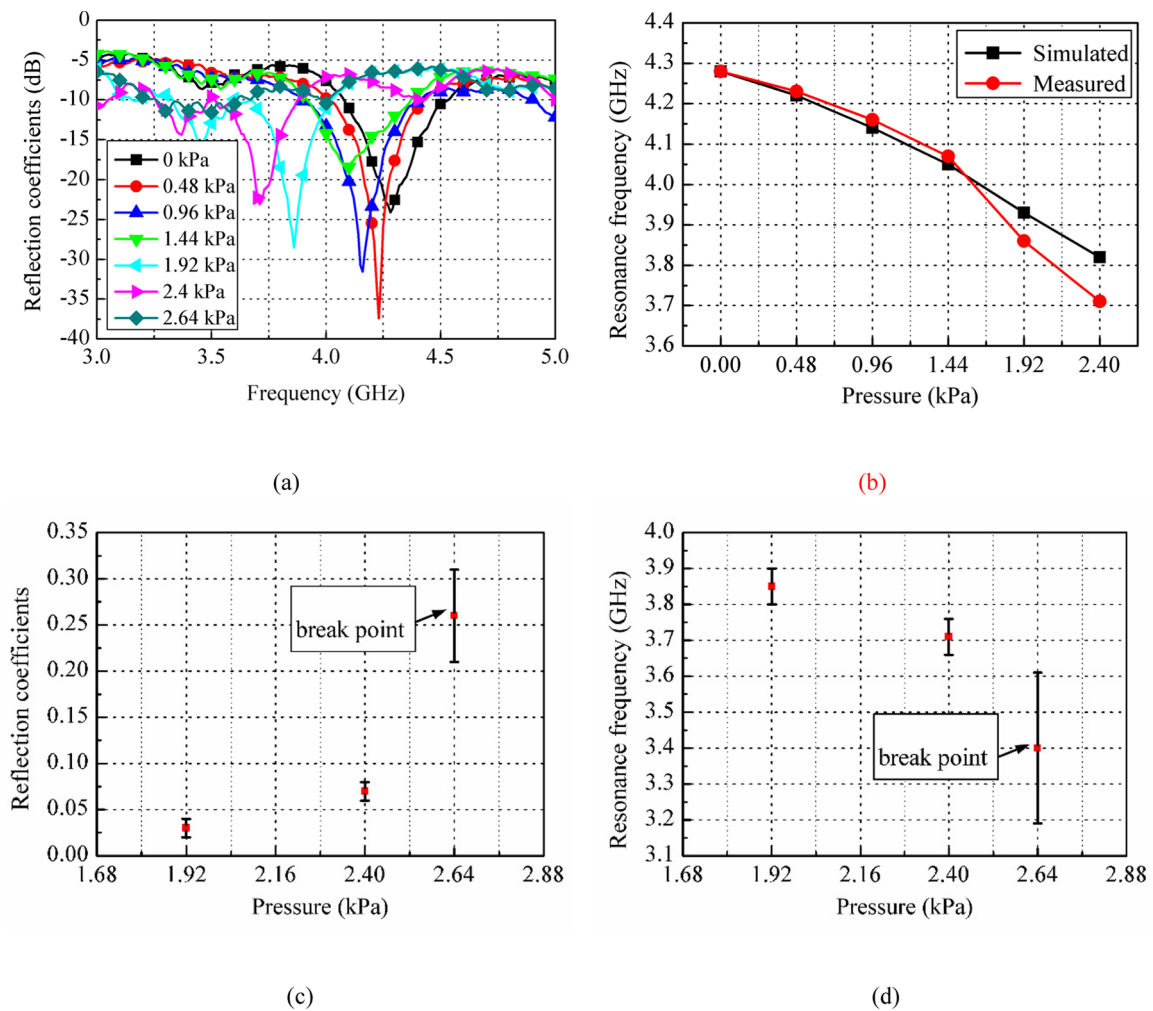


Fig. 10. Measurement results for the fabricated SIW pressure sensor: (a) reflection coefficients with respect to pressure, (b) simulated and measured resonance frequencies with respect to pressure, (c) reflection coefficients (linear) including variation with respect to pressure, and (d) resonance frequency including variation with respect to pressure.

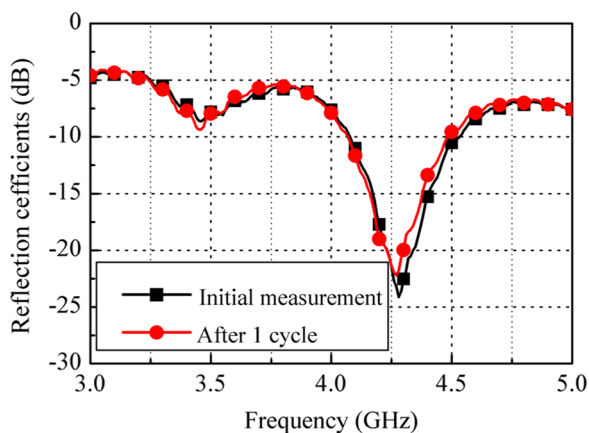


Fig. 11. Dynamic stability for the fabricated SIW pressure sensor.

material cost compared with traditional subtractive manufacturing.

Additive manufacturing processes are generally somewhat more environment friendly than traditional subtractive approaches, as there are no harmful chemicals involved. Traditional fabrication generally includes at least one etching step, which generates poisonous and harmful solutions contains copper and iron. Moreover, additive processing is fast and scalable, e.g. the proposed sensor could be

automatically fabricated in just a few hours. Industrial multi-printhead inkjet printing systems and automated 3D printing production lines would allow cost-effective large scale production.

5. Conclusion

This paper proposed an EM based planar SIW pressure sensor fabricated using 3D printed flexible photopolymer resin with an inkjet printed conductive pattern. The proposed pressure sensor was based on a TE_{101} mode SIW cavity with circular cylinder and four bridges inserted into the centre for perturbation. Capacitive coupling within the SIW cavity due to different pressure on the cylinder shifts the resonance frequency. Experimental results showed resonance frequency decreased from 4.28 to 3.71 GHz, as pressure increased from 0 to 2.4 kPa. Sensor sensitivity = 2.4×10^8 Hz/kPa, with stable frequency change over 100 repeats. The simulated and measured resonance frequencies with respect to pressure level have good agreement. Despite the narrow dynamic range, the proposed sensor showed good linearity and sensitivity. The additive manufacturing fabrication route for the proposed sensor is eco-friendly and could be rapidly implemented at relatively low cost.

Declaration of Competing Interest

The authors have no conflicting interests.

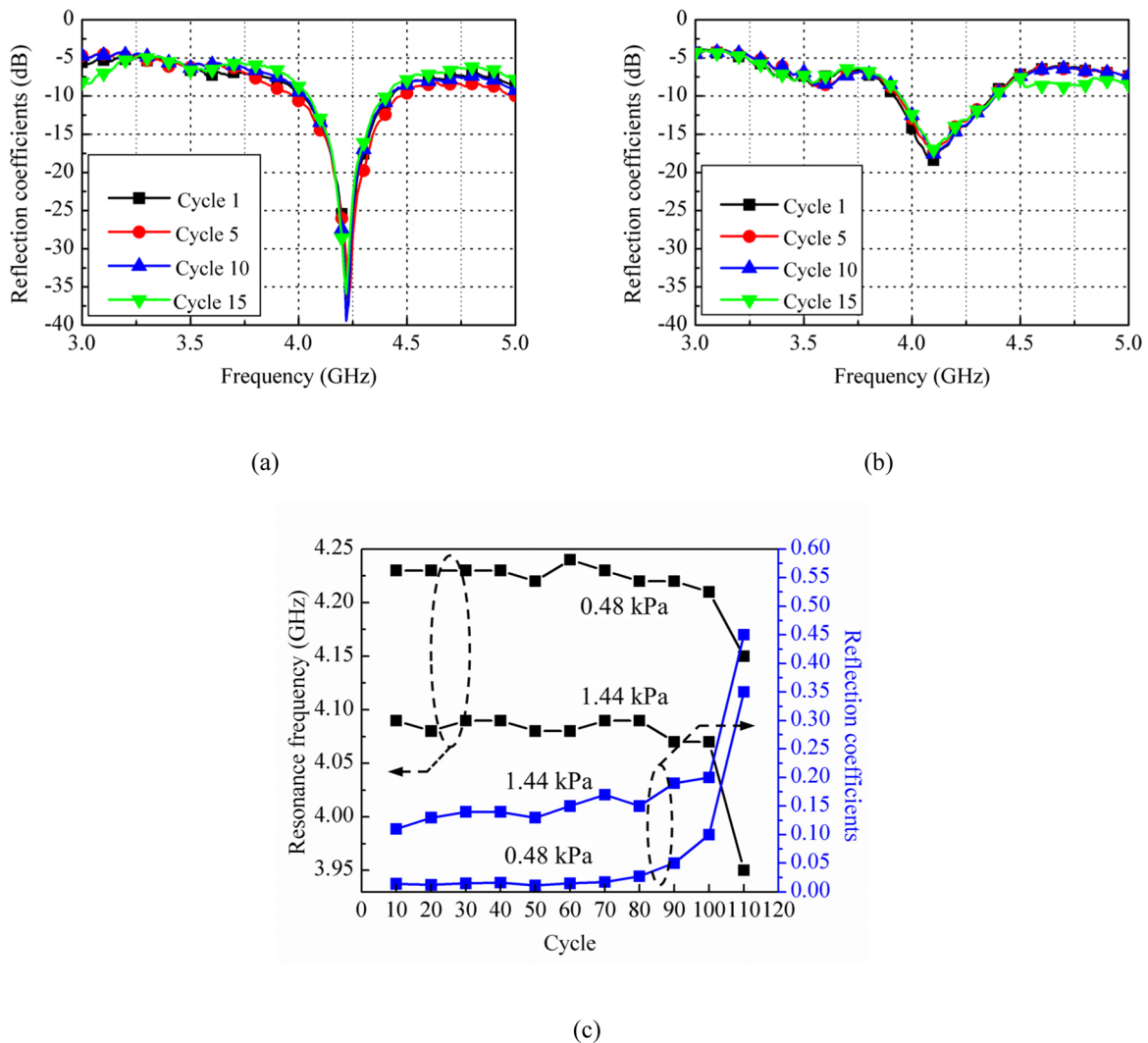


Fig. 12. Fabricated SIW pressure sensor repeatability at (a) 0.48 and (b) 1.44 kPa; (c) resonance frequency and reflection coefficients with respect to cycle.

CRedit authorship contribution statement

Yeonju Kim: Methodology, Validation, Formal analysis, Data curation, Software, Writing - original draft, Writing - review & editing,

Visualization. **Yepu Cui:** Methodology, Data curation, Software, Resources, Writing - original draft, Writing - review & editing, Visualization. **Manos M. Tentzeris:** Investigation, Methodology, Resources, Supervision, Project administration. **Sungjoon Lim:**

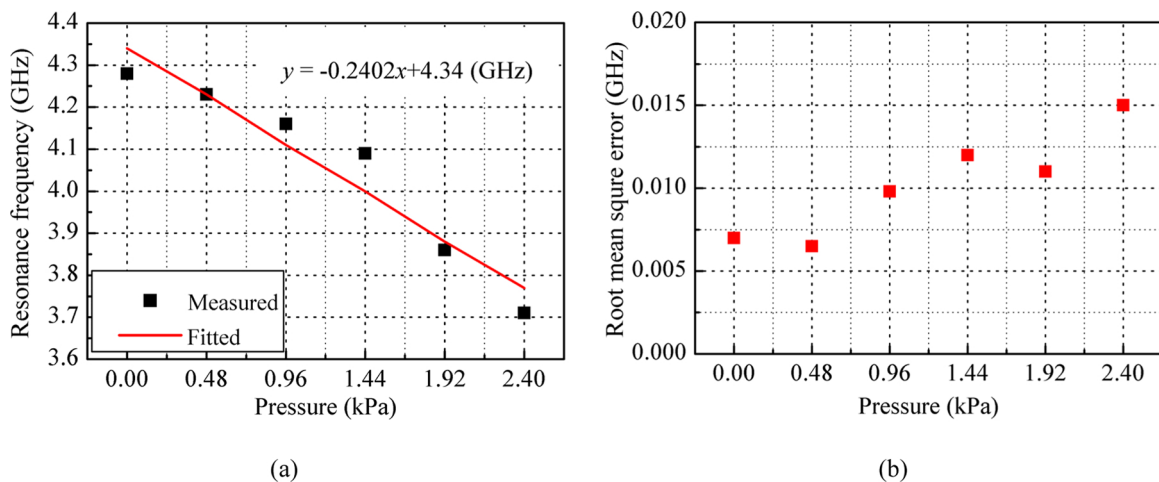


Fig. 13. Fabricated SIW pressures sensor (a) relationship between the resonance frequency and pressure level with the fitted curve (b) root mean square error (RMSE) with respect to pressure.

Table 3
Comparison of the proposed and current RF pressure sensors.

	Sensor material	Sensitivity	Dynamic range	Process	Cost
This paper	Resin, silver ink	2.40×10^8 Hz/kPa	0–2.40 kPa	Simple	Low
Li et al. [12]	Ceramic, platinum paste	1.55×10^3 Hz/kPa	0–20 kPa	Complicated	High
Luo et al. [13]	PLLA, Zn/Fe, Kapton film	3.9×10^4 Hz/kPa	0–20 kPa	Complicated	High
Akar et al. [14]	Silicon, glass	1.60×10^5 Hz/mmHg	0–50 mmHg	Complicated	Average
Xue et al. [15]	SU-8, Au, silicon	1.083×10^6 Hz/mmHg in air 6.83×10^5 Hz/mmHg in saline	0–60 mmHg	Complicated	Average

*10 mmHg \approx 1.33 kPa.

Conceptualization, Methodology, Investigation, Supervision, Project administration, Funding acquisition.

Korea (NRF) grant funded by the Korea government (MSIP) (No. 2017R1A2B3003856)

Acknowledgment

This work was supported by the National Research Foundation of

Appendix A

We used the finite element numerical method in COMSOL to obtain the results shown in Fig. 4. FEM is a numerical method for solving structural analysis and electromagnetic potential problems. To investigate pressure sensor elastic material characteristics with respect to height change, we first created the mesh shown in Fig. A1. We then expressed the relationship between stress and strain, and a set of algebraic equations for steady state was derived as

$$-\nabla \cdot \sigma = F \nu \tag{A1}$$

$$\sigma = J^{-1} S F^T, F = (1 + \nabla u), J = \det(F), \tag{A2}$$

$$S - S_0 = C : (\epsilon) \tag{A3}$$

$$\epsilon = \frac{1}{2} [(\nabla u)^T + \nabla u + (\nabla u)^T \nabla u] \tag{A4}$$

and

$$C = C(E, \nu) \tag{A5}$$

where σ is the stress tensor, F is body force, u is a unit vector, C is the stiffness tensor, ϵ is the strain tensor, E is Young’s modulus, and ν is Poisson’s ratio. We also used

$$\sigma \cdot n = F_a, F_a = -\rho n \tag{A6}$$

where n is the normal vector, and ρ is pressure, to calculate height change with respect to pressure.

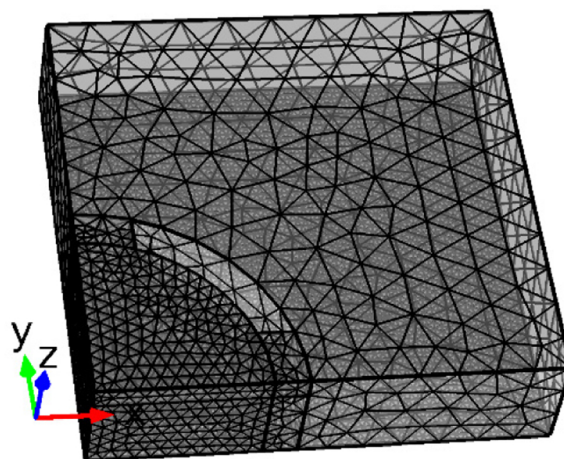


Fig. A1. Mesh structure for analysing pressure sensor characteristics.

Appendix B. Supplementary data

Supplementary material related to this article can be found, in the online version, at doi:<https://doi.org/10.1016/j.addma.2020.101225>.

References

- [1] L. Xu, W. He, S. Li, Internet of things in industries: a survey, *IEEE Trans. Ind. Informatics* 4 (2014) 2233–2243.
- [2] A. Al-Fuqaha, M. Guizani, M. Mohammadi, M. Aledhari, M. Ayyash, Internet of things: a survey on enabling technologies, protocols, and application, *IEEE Commun. Surv. Tutorials* 17 (2015) 2347–2376.
- [3] S. Amendola, R. Lodato, S. Manzari, C. Occhiuzzi, G. Marrocco, RFID technology for IoT-based personal healthcare in smart spaces, *IEEE Internet Things J.* 1 (2014) 144–152.
- [4] Y. Zang, F. Zhang, C. Di, D. Zhu, Advances of flexible pressure sensors toward artificial intelligence and health care application, *Mater. Horizon* 2 (2015) 140–156.
- [5] K. Lee, J. Lee, G. Kim, Y. Kim, S. Kang, S. Cho, S. Kim, J. Kim, W. Lee, D. Kim, S. Kang, D. Kim, T. Lee, Rough-surface-enabled capacitive pressure sensors with 3D tough capability, *Small* 13 (2017) 38–44.
- [6] X. Chen, J. Shao, N. An, X. Li, H. Tian, C. Xu, Y. Ding, Self-powered flexible pressure sensors with vertically well-aligned piezoelectric nanowire arrays for monitoring vital signs, *J. Mater. Chem. C* 3 (2015) 11806–11814.
- [7] T. Jones, M. Zarifi, M. Daneshmand, Miniaturized quarter-mode substrate integrated cavity resonators for humidity sensing, *IEEE Microw. Wirel. Compon. Lett.* 27 (2017) 612–614.
- [8] L. Catarinucci, R. Colella, L. Tarricone, Enhanced UHF RFID sensor-tag, *IEEE Microw. Wirel. Compon. Lett.* 23 (2013) 49–51.
- [9] R. Goncalves, S. Rima, R. Magueta, P. Pinho, A. Collardo, A. Georgiadis, J. Hester, B. Carvalho, M.M. Tentzeris, RFID-based wireless passive sensors utilizing cork materials, *IEEE Sens. J.* 15 (2015) 7242–7251.
- [10] S. Kim, Y. Kawahara, A. Georgiadis, A. Collado, M.M. Tentzeris, Low-cost inkjet-printed fully passive RFID tags for calibration-free capacitive/haptic sensor applications, *IEEE Sens. J.* 15 (2015) 3135–3145.
- [11] A. Abdulhadi, A. Denidni, Self-powered multi-port UHF RFID tag-based sensor, *IEEE J. Radio Freq. Identif.* 1 (2017) 115–123.
- [12] C. Li, Q. Tan, J. Xiong, P. Jia, Y. Hong, Z. Ren, T. Luo, J. Liu, C. Xue, W. Zhang, A noncontact wireless passive radio frequency (RF) resonant pressure sensor with optimized design for applications in high-temperature environments, *Meas. Sci. Technol.* 25 (2014) 1–10.
- [13] M. Luo, A. Martinez, C. Song, F. Herrault, M. Allen, A Microfabricated wireless RF pressure sensor made completely of biodegradable materials, *J. Microelectromech. Syst.* 23 (2014) 4–13.
- [14] O. Akar, T. Akin, K. Najafi, A wireless batch sealed absolute capacitive pressure sensor, *Sensors Actuators B Chem.* 95 (2001) 29–38.
- [15] N. Xue, S. Chang, J. Lee, A SU-8 based microfabricated implantable inductively coupled passive RF wireless intraocular pressure sensor, *J. Microelectromech. Syst.* 21 (2012) 1338–1346.
- [16] N. Lazaurs, S. Bedair, G. Smith, Creating 3D printed magnetic devices with ferrofluids and liquid metals, *Addit. Manuf.* 17 (2017) 15–21.
- [17] A. Walker, C. Prokop, B. Llynagh, B. Vuksanovich, K. Conner, J. Rogers, E. Mac Donald Thiel, Real-time process monitoring of core shifts during metal casting with wireless sensing and 3D sand printing, *Addit. Manuf.* 27 (2019) 54–60.
- [18] H. Kim, F. Torres, D. Billagran, C. Stewart, Y. Lin, T. Tseng, 3D printing of BaTiO₃/PVDF Composites with electric InSitu poling for pressure sensor applications, *Macromol. Mater. Eng.* 302 (2017) 1–6.
- [19] C. Liu, N. Huang, F. Xu, J. Tong, Z. Chen, X. Gui, Y. Fu, C. Las, 3D printing technologies for flexible tactile sensors toward wearable electronics and electronic skin, *Polymers* 10 (2018) 1–31.
- [20] H. Ota, et al., Application of 3D printing for smart objects with embedded electronics sensors and systems, *Adv. Mater. Technol.* 1 (2016) 1–8.
- [21] E. Suaste-Gomez, G. Rodriguez-Roldan, H. Reyes-Cruz, O. Teran-Jimenez, Developing an ear prosthesis fabricated in polyvinylidene fluoride by a 3D printer with sensory intrinsic properties of pressure and temperature, *Sensors* 16 (2016) 1–11.
- [22] B. Green, C. Guymon, Modification of mechanical properties and resolution of printed stereolithographic objects through RAFT agent incorporation, *Addit. Manuf.* 27 (2019) 20–31.
- [23] B. Cook, B. Tehrani, J. Copper, M.M. Tentzeris, Multilayer inkjet printing of millimeter wave proximity-fed patch arrays on flexible substrates, *IEEE Antennas Wirel. Propag. Lett.* 12 (2013) 1351–1354.
- [24] C. Sternkiker, E. Sowade, K. Mitra, R. Zichner, R. Baumann, Upscaling of the inkjet printing process for the manufacturing of passive electronic devices, *IEEE Trans. Electron Devices* 63 (2016) 426–431.
- [25] C. Li, Q. Tan, J. Xiong, P. Jia, Y. Hong, Z. Ren, T. Luo, J. Liu, C. Xue, W. Zhang, A noncontact wireless passive radio frequency (RF) resonant pressure sensor with optimized design for applications in high-temperature environments, *Meas. Sci. Technol.* 25 (2014) 1–10.
- [26] J. Lee, et al., Conductive fiber-based ultrasensitive textile pressure sensor for wearable electronics, *Adv. Mater.* 27 (2015) 2433–2439.
- [27] C. Gerlach, D. Krumm, M. Illing, J. Lange, O. Kanoun, S. Odenwald, A. Hubler, Printed MWCNT-PDMS-composite pressure sensor system for plantar pressure monitoring in ulcer prevention, *IEEE Sens. J.* 15 (2015) 3647–3656.
- [28] K. Brueckner, V. Cimalla, F. Niebelschutz, R. Stephan, K. Tonisch, O. Ambacher, A. Hein, Strain- and pressure-dependent RF response of microelectromechanical resonators for sensing applications, *J. Micromech. Microeng.* 17 (2007) 2016–2023.
- [29] J. Park, J. Kim, D. Kim, A. Shanmugasundaram, S. Park, S. Kang, S. Kim, M. Jeong, D. Lee, Wireless pressure sensor integrated with a 3D printed polymer stent for smart health monitoring, *Sens. Actuators B Chem.* 280 (2019) 201–209.
- [30] S. Cruz, D. Dias, C. Viana, L. Rocha, Inkjet printed pressure sensing platform for postural imbalance monitoring, *IEEE Trans. Instrum. Meas.* 64 (2015) 2813–2820.
- [31] C. Hong, Y. Zhang, L. Borana, Design, fabrication and testing of a 3D printed FBG pressure sensor, *IEEE Access* 7 (2019) 38577–38583.
- [32] L. Faller, W. Granig, M. Krivec, A. Abram, H. Zangl, Rapid prototyping of force/pressure sensor using 3D- and inkjet-printing, *J. Micromech. Microeng.* 28 (2018) 1–11.
- [33] D. Pozar, *Microwave Engineering*, fourth ed., John Wiley & Sons, Hoboken, 2012.
- [34] Z. Wei, J. Huang, J. Li, G. Xu, Z. Ju, X. Liu, X. Ni, A high-sensitivity microfluidic sensor based on a substrate integrated waveguide re-entrant cavity for complex permittivity measurement of liquids, *Sensors* 18 (2018) 1–17.
- [35] M. Bozzi, A. Georgiadis, K. Wu, Review of substrate-integrated waveguide circuits and antennas, *IET Microw. Antennas Propag.* 5 (2011) 909–920.
- [36] ANSYS High-Frequency Structure Simulator, ANSYS, Pittsburgh, PA, USA, 2016 Available: www.ansys.com.
- [37] M. Janezic, J. Jargon, Complex permittivity determination from propagation constant measurements, *IEEE Microw. Guid. Wave. Lett.* 9 (1999) 76–78.
- [38] (a) M. Mohsenizadeh, F. Gasbarri, M. Munther, A. Beheshti, K. Davami, Additively-manufactured lightweight metamaterial for energy absorption, *Mater. Des.* 139 (2018) 521–530; (b) J. Dizon, A. Espera, Q. Chen, R. Advincula, Mechanical characterization of 3D-printed polymers, *Addit. Manuf.* 20 (2018) 44–67.
- [39] “Formlabs choosing the right material”, <https://sourcegraphics.com/landing-pages/formlabs-choosing-right-material/>, (Accessed 12/01/2019).
- [40] J. Dizon, A. Espera, Q. Chen, R. Advincula, Mechanical characterization of 3D-printed polymers, *Addit. Manuf.* 20 (2018) 44–67.
- [41] P. Chen, F. Jia, H. Liu, Y. Han, Y. Zeng, X. Meng, Y. Xiao, G. Li, Effects of feeding direction on the hulling of paddy grain in a rubber roll huller, *Biosyst. Eng.* 183 (2019) 196–208.
- [42] M. Liang, W. Ng, K. Chang, K. Gbele, M. Gehm, H. Xin, A 3-D Luneburg lens antenna fabricated by polymer jetting rapid prototyping, *IEEE Trans. Antennas Propag.* 62 (2014) 1799–1807.
- [43] Y. Li, L. Ge, M. Chen, Z. Zhang, Z. Li, J. Wang, Multibeam 3-D-printed Luneburg lens fed by magnetoelectric dipole antennas for millimeter wave MIMO application, *IEEE Trans. Antennas Propag.* 67 (2019) 2923–2933.
- [44] J. Pourahmadazar, T. Denidni, Towards millimeter wavelength: transmission mode Fresnel zone plate lens antenna using plastic material porosity control in homogeneous medium, *Sci. Rep.* 8 (2018) 1–14.
- [45] Voronization Online, www.voronator.com, (Accessed on 02/28/2020).
- [46] “Using flexible resin”, https://support.formlabs.com/s/article/Using-Flexible-Resin?language=en_US, (Accessed on 07/27/2019).
- [47] B. Tehrani, B. Cook, M.M. Tentzeris, Inkjet-printed 3D interconnects for millimeter-wave system-on-package solutions, *IEEE MTT-S International Microwave Symposium (IMS)*, (2016), pp. 1–4 San Francisco CA.
- [48] Y. Cui, A. Nauroze, M.M. Tentzeris, Novel 3D-printed reconfigurable origami frequency selective surfaces with flexible inkjet-printed conductor traces, *IEEE MTT-S International Microwave Symposium (IMS)*, (2019), pp. 1367–1370 Boston MA U.S.A..
- [49] A. Arias, J. Mackenzie, I. McCulloch, J. Rivnay, A. Salleo, Materials and applications for large area electronics: solution-based approaches, *Chem. Rev.* 110 (2010) 3–24.